AFM Probing of Thermal Activation of Molecularly Linked Nanoparticle Assembly

**Jin Luo,**[†] **Vivian W. Jones,**[‡] **Li Han,**[†] **Mathew M. Maye,**[†] **Nancy N. Kariuki,**[†] **and Chuan-Jian Zhong*,**[†]

Department of Chemistry, State University of New York at Binghamton, Binghamton, New York 13902, and 3M Corporate Analytical Technology Center, 3M Center, St. Paul, Minnesota 55144-1000

Received: November 12, 2003; In Final Form: April 19, 2004

The ability to control the size and the spatial properties of nanoparticle catalysts on the surface of a substrate or support material is critical in exploiting the unique activity of catalysts at the nanoscale. We report herein new findings of an atomic force microscopic investigation of the thermal activation of molecularly wired core−shell nanoparticle assemblies on flat surfaces toward the development of the ability of size and spatial control. Gold nanocrystals of ∼2-nm core size capped by alkanethiolate shells were assembled by covalent or hydrogen-bonding linkages onto mica and graphite substrates as a model system. The results show that the particle size and interparticle spatial properties are highly dependent on the chemical and physical nature of the linker molecule and the substrate. Such dependence is inherently linked to the surface mobility, surface tension, and adsorption energy of nanoparticles on the substrate, which are supported by the assessment based on the theoretical modeling of the thermally induced sintering process. The surface mobility and consequent size evolution can be effectively influenced by manipulating the surface property or morphology of the substrate and that of the nanoparticles (e.g., functional groups, hydrophobicity, surface steps, etc.). The implications of our findings on the controlled processing of nanostructures on catalyst-support materials and the fine tuning of the catalytic or electrocatalytic activities are also discussed.

Introduction

The ability to harness the large surface area-to-volume ratio and the unique surface properties of nanoparticles in the <10-nm size range, especially in heterogeneous catalysis, is a major driving force in both fundamental research and practical applications of nanoparticle catalysts. It is this size range over which metal particles undergo a transition from atomic to metallic properties. The discovery of the high catalytic activity of gold in sizes below 5-nm diameter toward CO oxidation[1−4] has changed the traditional perception of gold as a catalyst. The emerging global interest in gold nanoparticle-based catalysts[5] has led to the realization that a combination of factors including size, support, and particle-support interactions is responsible for the unique catalytic properties of gold nanoparticles. A key challenge for the fundamental understanding of nanometer-sized gold as a catalyst is the control of particle size and the prevention of the inherent aggregation propensity. Because of the lack of ability to control size, shape, surface, and interparticle spatial properties, the structure−activity relationships of gold nanoparticle catalysts, including many commercial catalysts, are poorly understood. The recent exploration of core−shell-type nanoparticles, which can be broadly defined as a core and a shell of different matters in close interaction, including inorganic/organic, inorganic/inorganic, organic/organic, and inorganic/biological combinations,[6−11] provides intriguing pathways to address issues related to the challenge. The use of such nanoparticles as building blocks for catalytic materials takes advantage of the diverse attributes, including size monodisper-

SCHEME 1: Schematic Illustration of the Thermal Activation of a Core−Shell-Type Nanoparticle Assembly on a Planar Substrate Surface
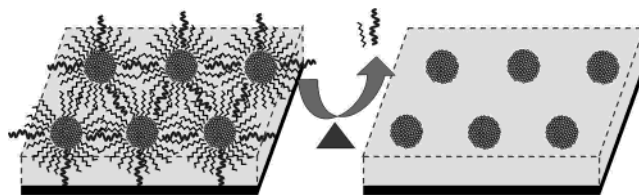
sity, processibility, solubility, stability, and self-assembly capability.[9,12−13]

Although the use of high-surface-area support materials is essential for many practical applications of nanoparticles in catalysis, the study of nanoparticle catalysts supported on a planar substrate is important for the fundamental understanding of the detailed nanostructure evolution or reconstitution with the help of advanced surface analytical tools (e.g., scanning probe microscopy). Consider the assembly of the molecularly capped/wired nanoparticles onto a desired support platform (Scheme 1). The assembly of the shell-capped nanoparticles involves the use of molecular wires or linkers and is activated by the partial or complete removal of the shell/linker molecules. A key element of this approach is the ability to control the size, surface composition, and interparticle spatial properties. To achieve this ability, it is important that we understand the relationship between the nanostructural properties and the surface or interfacial interactions under various chemical or physical conditions, which is the focus of this work.

The control and manipulation of the particle size and spatial properties of monolayer-capped nanoparticles on a surface are inherently linked to controllabilities in assembly, activation, and reconstitution of the core and shell components. We have

---

  * Corresponding author. Phone: 607-777-4605. E-mail: cjzhong@binghamton.edu.
  [†] State University of New York at Binghamton.
  [‡] 3M Corporate Analytical Technology Center.

demonstrated in our laboratory the assembly of gold-based nanoparticles by molecular wiring or linking and the subsequent activation by electrochemical[14,15] and thermal routes.[16] The electrochemical activation path is effective,[14−15] but it requires the use of a supporting electrolyte, which could limit its utility. The thermal activation path is a temperature-controlled removal of organic capping/linking components, leaving the nanocrystal cores behind. This path is both effective and convenient[16−17] and has in fact been explored in a number of recent related studies, including the thermolysis of metal−carboxylate bridged gold nanoparticles[18] for preparing conductive materials, thermal treatment of surfactant-capped Pt/Ru nanoparticles[19] and Pt-Ru$_5$C(CO)$_{16}$[20] on carbon support, polymer-mediated assembly of Pd on SiO$_2$ nanoparticles,[21] and dendrimer-mediated assembly of metal nanoparticles[22] for preparing catalysts. Currently, there is, however, little understanding of how the interparticle spatial and surface properties evolve thermally in a controllable way. This understanding is very important for the preparation of highly active, selective, and stable metal nanoparticle catalysts. This aspect has recently attracted both fundamental and practical interest in fuel cell catalysis.[5,17,23−24] In this paper, we present new findings of an atomic force microscopy (AFM) investigation of the thermal activation of alkanethiolate-linked gold nanoparticles on planar substrates. Our focus is to establish the fundamental understanding of the size and spatial evolution of metal nanoparticles with different molecular capping/linking properties on substrates with different chemical and physical natures.

Experimental Section

Chemicals. Decanethiol (DT, 96%), hydrogen tetrachloroaurate (HAuCl$_4$, 99%), tetraoctylammonium bromide (TOABr, 99%), 11-mercaptoundecanoic acid (MUA, 95%), 15-mercaptohexadecanoic acid (MHA, 90%), and 1,9-nonanedithiol (NDT, 95%) were purchased from Aldrich and used as received. Other chemicals included hexane (99.9%) and toluene (99.8%) from Fisher and methanol (99.9%) and ethanol (99.9%) from Aldrich. Water was purified with a Millipore Milli-Q water system.

Synthesis. Gold nanoparticles of 2-nm core size (Au$_{2\,nm}$, 1.9 ± 0.7 nm) encapsulated with DT monolayer shells were synthesized using Schiffrin's standard two-phase protocol[6] and modifications for synthetic control.[7] Details for the synthesis of our nanoparticles were recently described.[8] Gold nanoparticles of larger core sizes (4−6 nm) were derived from the Au$_{2\,nm}$ particles by a thermally activated processing route in a concentrated solution that was recently developed in our laboratory.[8] In this work, we largely focus on gold nanoparticles of ∼2-nm core sizes.

Preparation. The preparation of NDT- and MUA-linked assemblies of gold nanoparticles on a planar substrate followed the same procedure as recently reported,[25] except for a major difference in the concentrations of the constituents. In the typical procedure, the NDT or MUA thiols were mixed with DT-capped gold nanoparticles in a hexane solution, typically 3 mM NDT + 5−10 μM Au$_{2-nm}$ for an NDT-Au$_{2\,nm}$ assembly and 0.3 mM MUA + 5−8 μM Au$_{2\,nm}$ for an MUA-Au$_{2\,nm}$ assembly. The nanoparticle concentrations were determined by spectrophotometric calibrations and the assumption of an octahedra model for the average shape of the nanoparticles.[25,26]

The nanoparticles were assembled as a thin film on different substrates, including freshly cleaved mica and HOPG (highly ordered pyrolytic graphite) sheets by the exchange−cross-linking−precipitation route using NDT or MUA as a linking or wiring agent.[25,26] The organic components in the thin film

assembly consist of both NDT or MUA (wiring agent) and DT (capping agent) molecules, with the relative ratio depending on the extent of ligand exchange.[27,28] The general preparation involves the immersion of the substrate into a solution of nanoparticles and cross-linking agents at room temperature. The substrates were immersed vertically in the solution to ensure that the film was free of powder deposition. Upon emersion of the substrate from the assembling solution, the thin film was immediately and thoroughly rinsed with hexane and dried under nitrogen or air before characterizating. The thickness (or coverage) was controlled by assembling time and monitored by measurements of surface plasmon resonance absorbance using UV−vis spectrophotometry and measurements of mass loading using a quartz-crystal microbalance.[26] The thickness of the thin films tested ranged from submonolayer to multilayer coverages.

Thermal treatment of the nanoparticle assemblies was performed using a muffle furnace under air. The controlled temperature ranged from 50 to 400 °C. The temperature was controlled to within ±10 °C.

Instrumentation and Measurement. A Multimode Nano-Scope IIIa (Digital Instruments, Santa Barbara), equipped with an E scanner (maximum scan size: 16 μm), was utilized for AFM imaging. The capability of tapping mode (TM) AFM allows for imaging with minimum disruption to the nanostructures. Standard silicon tapping cantilevers (nanosensors) were used with a force constant of 40N/m (TESP). The probe has a nominal tip radius with a curvature of ∼10 nm. All images were acquired in TM. The instrument was calibrated by imaging standard calibration gratings.

The samples were subjected to in-situ heating (as described in the following sections) on a JVH integrated scanner/hot stage manufactured by Digital Instruments (maximum scan size 200 μm). The JVH scanner (and tip heater) works in conjunction with the Multimode Nanoscope IIIa. The same area was imaged in TM before and after being heated. The probes used were 225-μm-long single-crystal Si nanosensors with a force constant of 40 N/m AFM probes (LTESP). Because of the bimetallic bending behavior common to coated cantilevers, the probes used for in situ experiments were uncoated single-crystal Si nanosensors.

Results and Discussion

Using surface spectroscopic, probe microscopic, and thermogravimetric techniques, we have recently shown that the capping/linking molecular shells can be removed by electrochemical and thermal treatments.[15−16] In the case of thermal activation, we found that the heating of the nanoparticles under ambient conditions in the temperature range of 200−300 °C can effectively remove the shell/linking materials. To gain an in-depth understanding of the consequent evolution of the morphology of the assembled nanoparticles before and after the thermal activation, we carried out a systematic study using AFM under both ex-situ and in-situ conditions.

As illustrated in Figure 1, the change in size of individual nanoparticles (e.g., DT-capped Au$_{2\,nm}$) cast on mica as a result of the thermal treatment at 225 °C can be detected by the change in the height data of the AFM images. Before the heating treatment (Figure 1A), the average particle size determined from the cross-section data (height) is consistent with the expectation for the sum of the core diameter (2.0 nm) and the shell molecular length times a factor of 2 (∼2.5 nm).

After the thermal treatment (Figure 1B), the relative position of the nanoparticles remains unchanged. As evidenced by the

Molecularly Linked Nanoparticle Assembly

J. Phys. Chem. B, Vol. 108, No. 28, 2004 **9671**
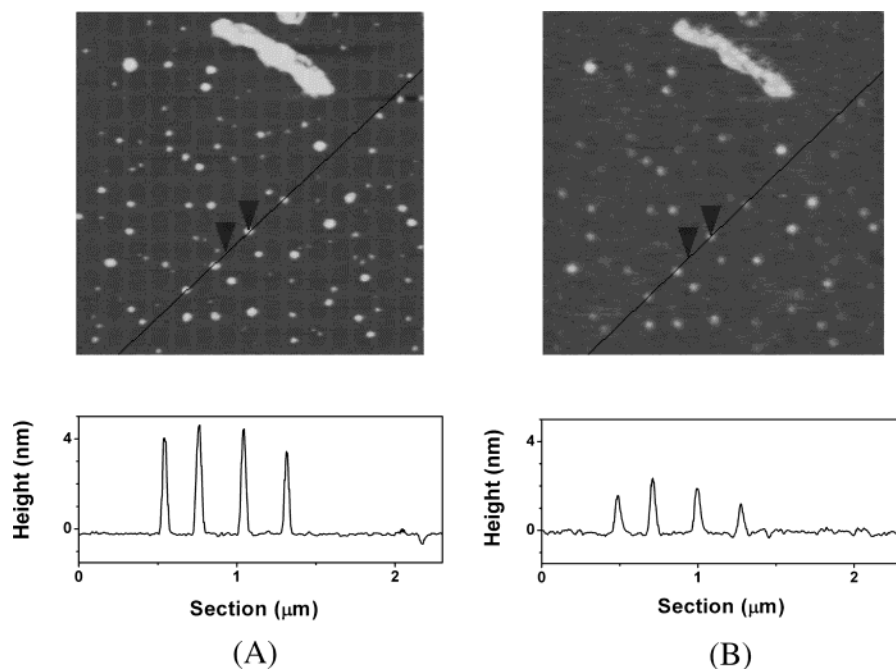
Figure 1. In-situ AFM images ($2 \times 2\ \mu m^2$) for DT-capped $Au_{2\ nm}$ on mica before (A) and after (B) thermal treatment at 225 °C for 30 min (image acquired after cooling to room temperature). The top bar of the nanoparticles serves as an internal location feature. The cross-section view corresponds to the line drawn in the image.
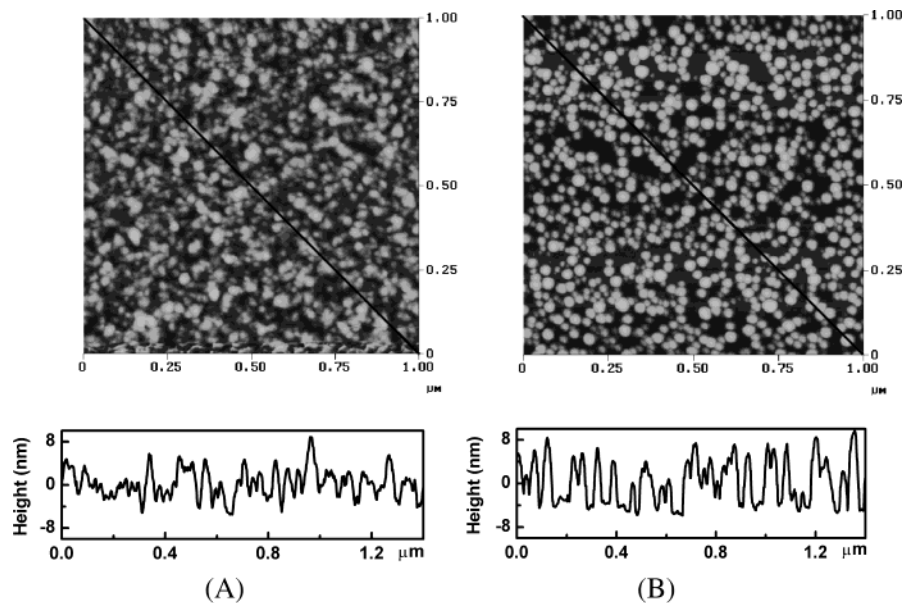

Figure 2. AFM images ($1 \times 1\ \mu m^2$) of NDT-$Au_{2\ nm}$/mica before (A) and after (B) thermal treatment at 250 °C for 30 min. (The image was acquired after cooling to room temperature.) The cross-section view corresponds to the line drawn in the image.

cross-section data, the particles displayed a clear shrinkage in size. The shrinkage is due to the removal of the capping-shell molecules. In this case, there is no apparent aggregation of the nanocrystal cores because the particles are widely separated and the adhesion (adsorption) of nanocrystals to the surface of mica is quite strong. We next closely examined effects of the linking molecule and the substrate on the morphological evolution of the assembled nanoparticles.

Effect of the Linker Molecule. An important function of the linking molecule is to define some of the interparticle properties for the as-formed nanoparticle assembly. Because the linking/capping molecules are removed by the heating treatment, as evidenced by IR and XPS studies,[16] the question is whether

this initial spatial definition has any impact on the evolution of nanoparticles. A typical set of ex-situ AFM images for an ~2-equiv layer of NDT-Au_{2-nm} films on mica before and after thermal treatment at 250 °C is shown in Figure 2. In this case, we chose to show the data for a sample with slightly more than one monolayer because the particles are densely packed and serve as a better example for comparing the overall morphological change under the ex-situ sampling condition. The coverage was determined by using the absorbance measurement of the surface-plasmon resonance band and the quartz-crystal microbalance measurement of the mass loading. Features of the assembled particles display an apparent lack of resolution at the edges of the particles due to a combination of the tip−sample
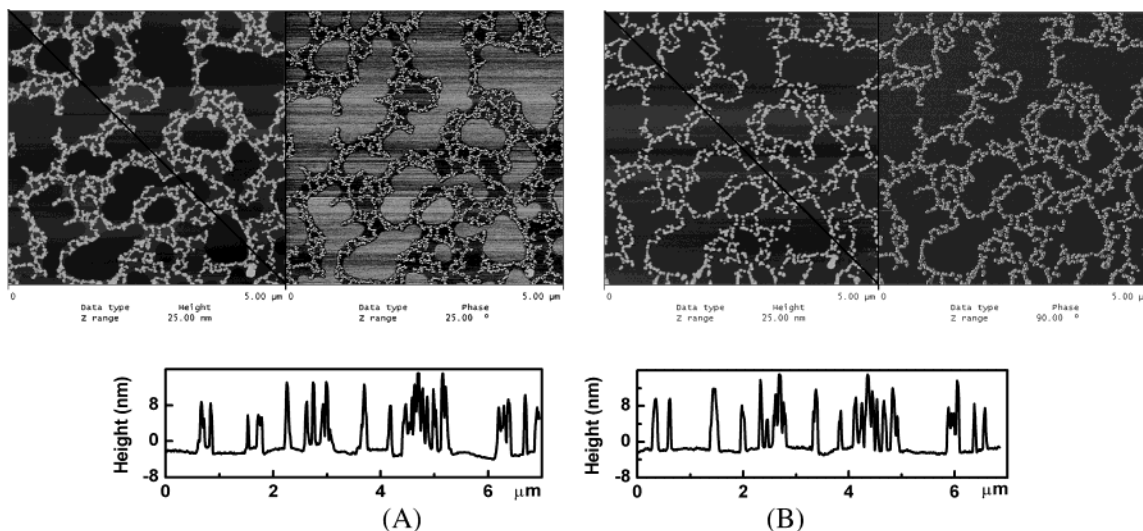
Figure 3. In-situ AFM images ($5 \times 5 \ \mu m^2$) of an NDT-Au$_{2 \ nm}$/mica film before (A) and after (B) heating to 225 °C for 30 min. (The image was acquired after cooling back to room temperature.) In each case, both topography (left) and phase (right) images are included for comparison. The cross-section view corresponds to the line drawn in the topography image.

convolution[29] and the shell−shell interaction. The average height of ∼7 nm corresponds to the superimposition of ∼2 nanoparticles. In our actual measurement of the height, we used several sets of cross-section data that also contain the substrate's background. After the treatment, the edges of the nanoparticles appear to be much better resolved because of the removal of the soft shell. The average height of the particles (8.9 ± 2.9 nm) is somewhat increased, indicating a certain degree of localized aggregation of the superimposed nanoparticles. Similar features were also observed for submonolayer-coverage samples where particles with clustering features are present (data not shown).

In-situ AFM imaging experiments provided important insights into the mechanism at hand. The experiments were performed by directly mounting the sample on a heated piezo stage. This enabled the same particle or particle assemblies to be monitored before and after the heating treatment. Figure 3 shows a typical set of AFM images for NDT-Au$_{2 \ nm}$ films on mica before and after the thermal treatment at 225 °C for 30 min. We chose to show the data for a sample with a submonolayer coverage because the particles are less-densely packed to allow for a detailed comparison of the morphological changes. The assembled particles are clustered into wire or chainlike morphologies. The cross-section data suggest that the nanoparticles form layers that are ∼3 nanoparticles thick on average. The edges of individual nanoparticles are not well resolved (Figure 3A). After the thermal treatment, the edges of individual particles are better resolved. Interestingly, the chainlike interparticle morphology remains intact. The removal of the thiolate shell at this temperature was supported by the TM-phase imaging data, which reveals that the dark phase contrast that is normally attributed to a softer material is absent for the thermally treated assembly (Figure 3B) compared to the as-prepared assembly (Figure 3A). On the basis of the comparison between the phase and topography images, we found that the height of the corresponding region in topography images, ∼1 nm, is consistent with the thickness of the organic layer. The corresponding phase image was darker than that for the nanoparticle features. It is generally known that soft materials, as is the case here, cause more phase shift than hard or stiffer materials. The origin of the darker phase signal can thus be attributed to the presence of thiolate chains. The height analysis of the cross-section data reveals average particle sizes of 11.1 ± 3.9 nm (Figure 3A)

and 13.1 ± 3.4 nm (Figure 3B), respectively, suggesting a small change in size. The small increase in size is believed to be due to a localized aggregation, largely from superimposing particles. The largely unchanged interparticle spatial feature in the lateral plane demonstrates that the interparticle spatial property can be controlled even if there is a local aggregation from the superimposed nanoparticles. The combination of the initial molecular capping/wiring and the subsequent adhesive interaction of the particle to the substrate must have played an important role in the spatial fixation.

The relatively small changes in particle size (measured by height) and interparticle spatial features in the lateral plane have demonstrated that the interparticle properties are controllable in the presence of a local sintering of the clustered nanoparticles. We note that the thermally activated particles were catalytically active toward methanol oxidation[16] similar to or slightly higher than the activity by electrochemical activation.[14] It is important to point out that the x−y feature sizes cannot be used to evaluate the changes in the number of particles in the clustered features because of the limitation of the AFM lateral resolution. The imaged lateral sizes before and after the removal of the capping/ linking molecules cannot be compared directly, especially for our image feature's lateral sizes in the 10−40-nm region. As such, the clustered feature of nanoparticles in the image before shell removal may in fact have a lot of particles, but they could not be resolved.

MUA-linked Au nanoparticle films on mica were also examined. Figure 4 shows a representative set of AFM images of an MUA-Au$_{2 \ nm}$ (∼1.6 layers) before and after heating at 250 °C. In this case, densely packed monolayer-coverage domains are evident. The as-formed film exhibited bare holes (no particle coverage); the height measured from the cross-section data of the densely packed nanoparticle domains was ∼3.5 nm, closely comparable with the thickness of a single layer of the MUA-Au$_{2 \ nm}$ assembly. We note that it is often difficult to resolve individual nanoparticles for the MUA-Au$_{2 \ nm}$ assembly, even at smaller imaging sizes. Two related additional facts are (1) that we could easily resolve individual nanoparticles for NDT-linked nanoparticles and (2) that we were able to resolve individual nanoparticles for larger-sized and monodisperse nanoparticles (5−6 nm). Currently, we are not completely clear about the origin. In addition to the tip−sample convolution effect, the combination of the small particle size (less mono-

Molecularly Linked Nanoparticle Assembly

J. Phys. Chem. B, Vol. 108, No. 28, 2004 **9673**
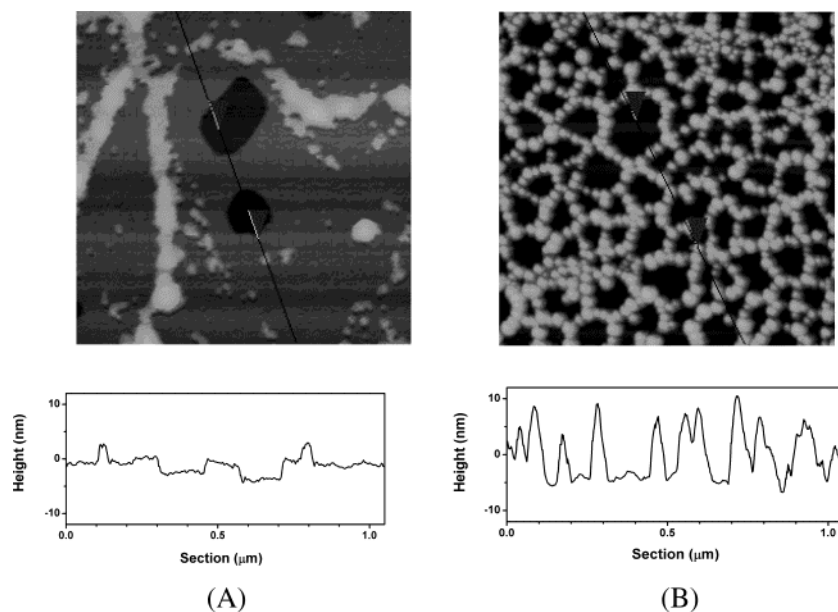
Figure 4. AFM images (1×1 μm^2) of MUA-Au$_{2\,nm}$/mica before (A) and after (B) thermal treatment at 250 °C for 30 min. (The image was acquired after cooling to room temperature.) The cross-section view corresponds to the line drawn in the image.
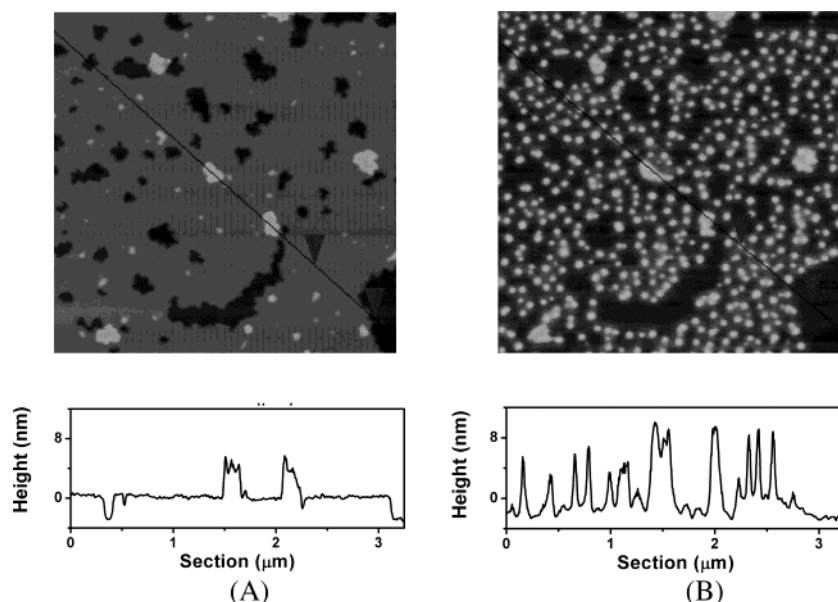
Figure 5. In-situ AFM images (2.5×2.5 μm^2) of a MUA-Au$_{2\,nm}$/mica before (A) and after (B) heating to 225 °C for 5 min. (The image was acquired after cooling back to room temperature.) The cross-section view corresponds to the line drawn in the image.

disperse) and the effect of the squeezed hydrogen-bonding or alkyl-chain interdigitation is believed to be operative, as recently proposed in a squeezed model for MUA-linked Au$_{6\,nm}$.[28] These effects could average out the height difference. After the thermal treatment, the film displayed a networklike feature composed of particles that were twice the original film's thickness. The average size of the particles is about 7 nm. This set of data indicates that the densely packed MUA-Au$_{2\,nm}$ nanoparticles have a higher tendency of local aggregation than the NDT-Au$_{2\,nm}$ nanoparticles. This set of data partially suggests that a densely packed system would aggregate more than a less-packed system, in addition to the effect of linker molecules.

Additional details of the morphological evolution were obtained by in-situ AFM imaging of an MUA-Au$_{2\,nm}$ film of ~1-layer thickness. Figure 5 shows a representative set of in-situ AFM images before and after heating at 225 °C. The assembled nanoparticles again form large domains of densely packed particles (as in Figure 4). In this case, we can see that

the particles after the heating treatment undergo significant local aggregation, forming individually isolated and larger-sized particles. The resulting particle sizes are relatively monodisperse (averaging ~8 nm).

It is clear not only that the morphology of the as-formed films is dependent on the nature of the linking molecules but also that the size features of the thermally evolved particles are dependent on the chemical nature of the linker molecules. This result suggests that interparticle interaction plays an important role in the thermally induced nanostructural evolution process. We next show that the morphological properties are also dependent on interactions between the particles and the substrate.

Effect of the Substrate. In the above imaging study, mica, a hydrophilic material, was used as the substrate. To probe the substrate effect, we now examine nanoparticle assemblies on HOPG, a hydrophobic substrate. Figure 6 shows a representative set of AFM data (before and after the heating treatment) for NDT-Au$_{2\,nm}$ on HOPG. In comparison to data shown earlier
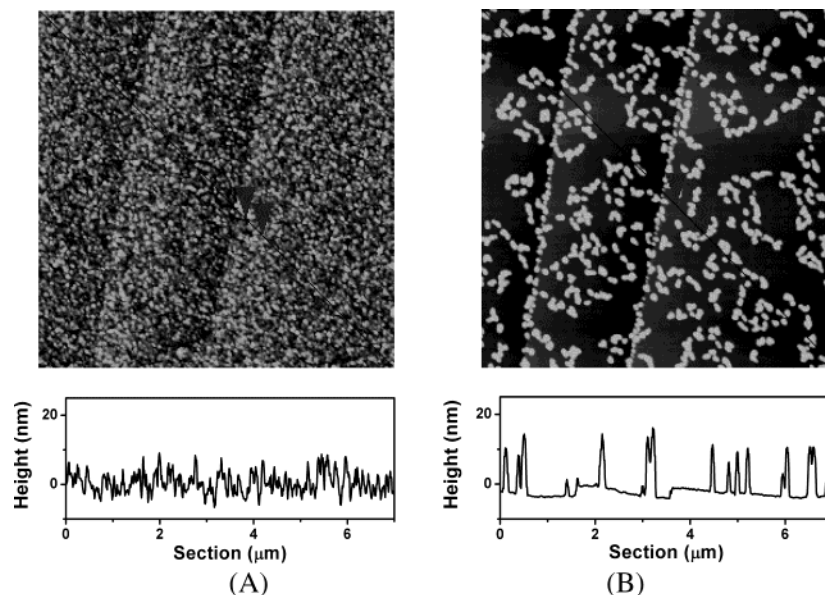
Figure 6. In-situ AFM images (5 × 5 μm^2) for NDT-Au$_{2\,nm}$ on HOPG before (A) and after (B) thermal treatment (225 °C, 5 min). The cross-section view corresponds to the line drawn in the image.

for similar films on mica, there are two important findings for the particle evolution. First, the as-formed nanoparticle assemblies (∼2 layers) display relatively uniform coverage on the HOPG surface, in contrast to the formation of domain features on the mica surface. This suggests that an important role is played by the hydrophobic interaction between the shell/linker component and the substrate. Second, the degree of aggregation of the particles after the thermal treatment exhibited several interesting differences between mica and HOPG. In general, the particles on HOPG showed a greater tendency of aggregation than those on mica.

Furthermore, the tendency of aggregation is found to be dependent on the nature of the linker molecules. Figure 7 shows a representative set of AFM data (before and after the heating treatment) for MUA-Au$_{2\,nm}$ on HOPG. It is evident that a relatively large fraction (∼90%) of the HOPG surface that was previously completely covered by nanoparticles becomes virtually bare after the heating treatment. It is also evident that the increase in particle sizes for the MUA-linked nanoparticles (Figure 7B) (average size ∼14 nm) is much larger than for the NDT-linked assembly (Figure 6B) (average size ∼10 nm). The average sizes were determined on the basis of the AFM cross-sectional data. Note that there are particles both inside and outside the naturally occurring trenches of HOPG. The particle aggregation is observed both inside and outside the trenches after the thermal treatment. These findings suggest that there is a higher surface mobility (or lower particle−substrate interaction) for the assembled particles on the hydrophobic HOPG surface in comparison with the hydrophilic mica surface. Similar conclusions have also been reached from our TEM characterizations of the morphology of nanoparticles on a carbon-coated Cu grid after the heating treatment.

An intriguing observation in the above set of data is that the nanocrystals are accumulated along step edges of the HOPG substrate after the heating treatment, forming wirelike features. This finding is remarkable because it indicates that the mobility of nanoparticles can be effectively regulated by the step edges on the substrate. We note that similar phenomena have also been observed for the dendrimer-mediated assembly of Pd nanoparticles on the HOPG substrate.[21b] A potential application

of such a step edge-guided nanoparticle movement on the surface is the formation of nanowires and other nanoscale shapes on surfaces that can be intentionally engineered (e.g., patterning). Part of our ongoing work involves developing of the control factors in such surface-guided nanowire formation and its application in catalysis and microelectronics.

Theoretical Consideration. To gain an in-depth understanding of the above findings, we considered conclusions drawn from theoretical modeling based on sintering theory. Theoretically, there are two possible pathways for thermally induced sintering and coagulation: (a) the sintering of small particles into larger-sized particles and (b) the agglomeration of small particles into a coagulated cluster.[30−32] The driving force for sintering can be described by the basic Gibbs−Thompson (G−T) relation, which relates the difference between the chemical potential of a metal atom in a particle of radius r, $\mu(r)$, and that in the bulk, $\mu(\infty)$, by eq 1:

$$\mu(r) - \mu(\infty) = \frac{2\gamma\Omega}{r} \tag{1}$$

where γ is the surface free energy of the metal and Ω is the bulk metal's volume per atom. In a recent study,[33] Campbell and co-workers demonstrated that the dependence of this energy on particle size is much stronger than predicted with the usual G−T relation. The size distribution depends on the interplay between the interparticle distances (or density) and the thermal mobility of metal atoms on the surface. A detailed delineation of the mechanistic aspects in terms of temperature, surface free energy, and particle size is thus important. There are essentially two limiting mechanisms:[31] (1) the diffusion of intact particles followed by coalescence and (2) the detachment of atoms from smaller particles followed by diffusion across terraces and reattachment to larger particles (Ostwald ripening). Although the determination of the size distribution as a function of annealing time could allow for the distinction of these two mechanisms, there is very limited knowledge for predicting how surface capping (which changes the surface tension) and wettability or adhesion (which controls the diffusion of metals) affect the sintering process. We considered the theoretical modeling to understand our experimental results better.

Molecularly Linked Nanoparticle Assembly

J. Phys. Chem. B, Vol. 108, No. 28, 2004 **9675**
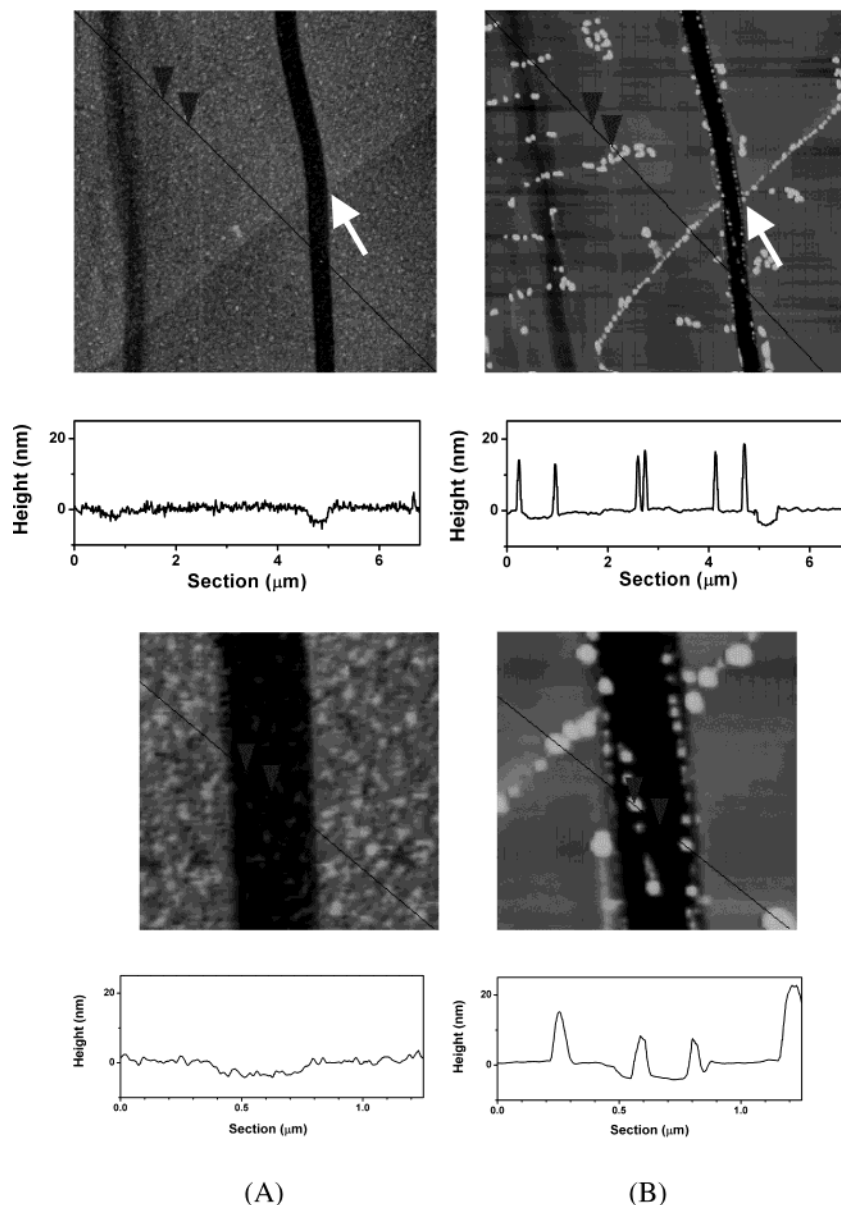
Figure 7. In-situ AFM images (top panel: $5 \times 5~\mu m^2$; bottom panel: $1 \times 1~\mu m^2$) for MUA-Au$_{2~nm}$ on HOPG before (A) and after (B) thermal treatment (225 °C, 5 min). The images in the bottom panel are magnified views of the indicated area. The cross-section view corresponds to the line drawn in the image. The two vertical trenchlike lines were naturally occurring features on HOPG, which served as internal features for imaging location.

Our simulation work is based on the model modified by Campbell and co-workers,[33]

$$\frac{dr}{dt} = \frac{2\gamma\Omega K}{kTr^2}(e^{-E_{tot}/kT})\left(\frac{r}{r^*} - 1\right) \quad (2)$$

where k is Boltzmann's constant, T is the temperature of the substrate, $r^* = 1/$(the average of $^1/_r$ for all particles), and $K = [(2~\sin~\theta)(\nu_P)(\Omega)]/[(2 - 3~\cos~\theta + \cos^3~\theta)(a)]$. θ is the equilibrium contact angle of the metal particles with the support surface, ν_P is the prefactor in the rate constant for the elementary step wherein a metal monomer diffusing along the edge of a particle leaves that particle to move out onto the support surface, and a is the interatomic spacing in the metal. The key relationship is that the rate of change of a metal particle's radius (r) is a function of the apparent activation energy E_{tot},[33]

$$E_{tot} = \Delta H_{sub} - (E_{ad}^{support} - E_{diff}^{support}) \quad (3)$$

where ΔH_{sub} is the metal's bulk sublimation enthalpy, $E_{ad}^{support}$ is the adsorption energy of a monomer on a support, and $E_{diff}^{support}$ is the activation energy for the diffusion of a metal monomer atom on a support. Using $\theta = 90°$, $\nu_P = 4 \times 10^{12}$ s^{-1}, heating rate = 1 K s^{-1}, and ΔH_{sub} (for Au)= 368 kJ/mol, a set of simulation results for the relative change in the average radius of the Au nanoparticles (for an initial $r = 1$ nm) on a flat substrate as a function of the temperature is shown in Figure 8.

Clearly, both of the surface energies ($E_{ad}^{support}$ and $E_{diff}^{support}$) and the surface tension (γ) have significant impacts on the size evolution. At constant γ, the rate of change of particle size with temperature is increased with decreasing E_{tot} (Figure 8A), whereas at constant E_{tot}, the rate of change of particle size with temperature is increased with increasing γ (Figure 8B). The experimental and theoretical results can be understood on the basis of comparisons to the relative activation energies and surface tensions (Table 1). The basic assumption in our
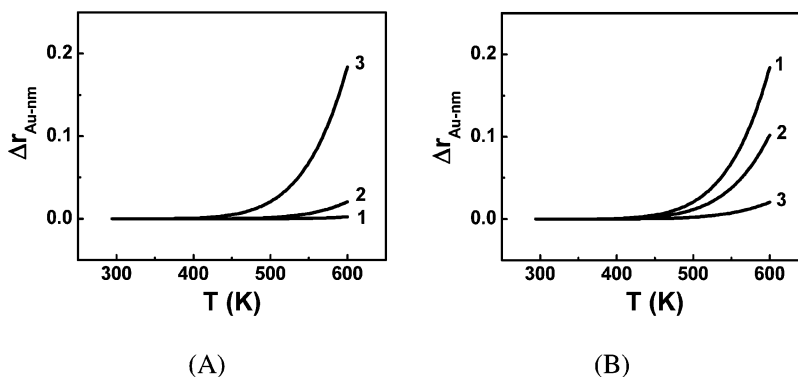
Figure 8. Simulation results for the relative change in the average radius of Au nanoparticles on a flat substrate as a function of the temperature on the basis of eq 2. (A) $\gamma = 90\ \mu J/cm^2$; $E_{tot} = 70$ (1), 60 (2), and 50 kJ/mol (3). (B) $E_{tot} = 50$ kJ/mol; $\gamma = 90$ (1), 50 (2), and 10 $\mu J/cm^2$ (3).

TABLE 1: Qualitative Comparison of Apparent Activation Energies and Surface Free Energies

	mica		HOPG
activation energy	E_{tot}	>	E_{tot}
surface free energy	NDT		MUA
	$\gamma\ (-CH_3)$	<	$\gamma\ (-CO_2H)$

assessment is that the adsorption energy is mainly dictated by the interaction of the monolayer-capped nanoparticle with the substrate, whereas the diffusion energy is largely determined by the interaction of gold nanocrystals with the substrate. This qualitative assumption is reasonable in view of our thermal-treatment condition near the organic-removal temperature ($\sim$225 °C), below which the organic shell is partially present and above which the shell is absent and aggregation occurs. The difference between $E_{tot}^{(HOPG)}$ and $E_{tot}^{(mica)}$ (from eq 3) can be written as

$$E_{tot}^{(HOPG)} - E_{tot}^{(mica)} = [\Delta H_{sub}^{(HOPG)} - \Delta H_{sub}^{(mica)}] - [(E_{ad}^{(HOPG)} - E_{diff}^{(HOPG)}) - (E_{ad}^{(mica)} - E_{diff}^{(mica)})]\ (4)$$

Because the bulk sublimation enthalpy should not be affected by the substrate in any significant way, we have

$$E_{tot}^{(HOPG)} - E_{tot}^{(mica)} = -[(E_{ad}^{(HOPG)} - E_{diff}^{(HOPG)}) - (E_{ad}^{(mica)} - E_{diff}^{(mica)})]\ (5)$$

Previous work[33] has indicated that $E_{ad} - E_{diff} > 0$. On the basis of the nature of the nanoparticle—substrate adsorption, that is, the predominant hydrophobic—hydrophobic interaction for the adsorption on HOPG and the hydrophobic—hydrophilic interaction for that on mica, it is evident that $E_{ad}^{(HOPG)} > E_{ad}^{(mica)}$. However, the reversal of the interaction nature for the diffusion property should lead to $E_{diff}^{(HOPG)} < E_{diff}^{(mica)}$. Therefore, we should have $E_{tot}^{(HOPG)} - E_{tot}^{(mica)} < 0$, that is, $E_{tot}^{(HOPG)} < E_{tot}^{(mica)}$. We note that the above qualitative analysis is yet to be confirmed by additional experimentation.

As such, the particle size on HOPG would increase more significantly than on mica with increasing temperature. This trend is indeed consistent with the in-situ AFM data showing a larger particle size on HOPG than on mica. Furthermore, this reduced surface mobility of gold nanocrystals on the mica surface is also consistent with the existence of a binding affinity of the surface hydroxyl groups to the metal surface. The binding affinity of surface sites on gold nanocrystals (with diameters of a few nanometers) to oxygen species has recently been shown (via theoretical calculations) to be much stronger than that on bulk gold surfaces.

For the same HOPG substrate (constant E_{tot} for Au on HOPG), the initial surface tension is larger for MUA-linked particles than for NDT-linked particles because of $\gamma(-CO_2H) > \gamma(-CH_3)$.[34] In this case, the particle size increases more significantly for MUA-linked particles according to Figure 8B. This is indeed in agreement with the AFM finding that shows larger particle sizes for MUA-$Au_{2\ nm}$ on HOPG. We note that our surface tension analysis is qualitative for comparing MUA- and NDT-linked nanoparticles at this time. Because the capping/linking shell structure consists of a mixed monolayer of DT/MUA or DT/NDT, it is difficult to directly use literature surface tension values.

The above findings are significant because they suggest that the manipulation of the surface free energy, wettability, or adhesion can impact the final size of the thermally processed nanoparticles on the surface. The free energy (γ) can be manipulated by changing the functional groups of the capping or interparticle-linking agents, whereas the surface energies ($E_{ad}^{support}$ and $E_{diff}^{support}$) can be manipulated by altering the surface functional groups, the hydrophobicity, or the binding properties of the substrate. When we compare the NDT- and MUA-linked particles, acid and methyl (and methylene) are at the interfaces. On the basis of the theoretical simulation and the qualitative analysis of eq 3, we mainly considered the initial aggregation of the nanoparticles, which involves energetic contributions from both shell—substrate and Au—substrate interactions.

Conclusions

We have shown that the thermal activation of the core—shell nanoparticles assembled on planar substrates by capping/linking molecules produces nanocrystals with a controllable size and interparticle morphology. The size and spatial properties depend on the nature of molecular linkers and the surface properties of the substrate. This dependence is inherently linked to the mobility or adhesion of nanoparticles on the surface. The results have provided important evidence for assessing the surface mobility and adhesion on the thermally induced morphological evolution of nanoparticles, which are additionally supported by theoretical modeling of the thermally induced sintering process in terms of activation energies for both surface adhesion and diffusion processes and surface free energy. We note that these thermally activated gold nanocrystals are electrocatalytically active toward methanol oxidation, which is of fundamental importance to fuel cell catalysis. We further note that the dependencies of the interparticle morphology on temperature, wiring structure, and substrate properties revealed in this work have important implications for a wide range of nanotechnological applications including catalysis, sensors, and nanoelec-

Molecularly Linked Nanoparticle Assembly

J. Phys. Chem. B, Vol. 108, No. 28, 2004 **9677**

tronics. The formation of controlled sizes or morphologies such as nanowires along surface steps by controlling the thermal treatment temperature and nanoparticle−substrate interaction properties of the core−shell nanoparticle assemblies is to our knowledge the first example of the potential surface engineering of nanostructures. We are currently developing an in-depth correlation of the thermally induced morphological evolution of the nanoparticles with surface energy, surface mobility, and molecular interactions and exploring their applications in catalysis and electrocatalysis.

References and Notes

(1) (a) Haruta, M. *Catal. Today* **1997**, *36*, 153. (b) Haruta, M.; Date, M. *Appl. Catal., A* **2001**, *222*, 427.

(2) Valden, M.; Lai, X.; Goodman, D. W. *Science* **1998**, *281*, 1647.

(3) (a) Sanchez, A.; Abbet, S.; Heiz, U.; Schneider, W. D.; Hakkinen, H.; Barnett, R. N.; Landman, U. *J. Phys. Chem. A* **1999**, *103*, 9573. (b) Heiz, U.; Sanchez, A.; Abbet, S.; Schneider, W. D. *Chem. Phys.* **2000**, *262*, 189. (c) Schmid, G.; Emde, S.; Maihack, V.; Meyer-Zaika, W.; Peschel, S. *J. Mol. Catal. A: Chem.* **1996**, *107*, 95.

(4) Bond, G. C.; Thompson, D. T. *Gold Bull.* **2000**, *33*, 41.

(5) (a) Landon, P.; Collier, P. J.; Papworth, A. J.; Kiely, C. J.; Hutchings, G. J. *Chem. Commun.* **2002**, 2058. (b) Hutchings, G. *New Directions in Gold Catalysis*, New Industrial Applications for Gold Conference of the World Gold Council, 2003. (c) Kung, H. H.; Kung, M. C.; Costello, C. K. *J. Catal.* **2003**, *216*, 425.

(6) Brust, M.; Walker, M.; Bethell, D.; Schiffrin, D. J.; Whyman, R. *J. Chem. Soc., Chem. Comm.* **1994**, 801.

(7) (a) Hostetler, M. J.; Wingate, J. E.; Zhong, C. J.; Harris, J. E.; Vachet, R. W.; Clark, M. R.; Londono, J. D.; Green, S. J.; Stokes, J. J.; Wignall, G. D.; Glish, G. L.; Porter, M. D.; Evans, N. D.; Murray, R. W. *Langmuir* **1998**, *14*, 17. (b) Hostetler, M. J.; Zhong, C. J.; Yen, B. K. H.; Anderegg, J.; Gross, S. M.; Evans, N. D.; Porter, M. D.; Murray, R. W. *J. Am. Chem. Soc.* **1998**, *120*, 9396.

(8) (a) Maye, M. M.; Zheng, W. X.; Leibowitz, F. L.; Ly, N. K.; Zhong, C. J. *Langmuir* **2000**, *16*, 490. (b) Maye, M. M.; Zhong, C. J. *J. Mater. Chem.* **2000**, *10*, 1895.

(9) Templeton, A. C.; Wuelfing, W. P.; Murray, R. W. *Acc. Chem. Res*. **2000**, *33*, 27, and references therein.

(10) Zhong, C. J.; Maye, M. M. *Adv. Mater.* **2001**, *13*, 1507.

(11) Schneider, J. J. *Adv. Mater.* **2001**, *13*, 529.

(12) (a) Hostetler, M. J.; Green, S. J.; Stokes, J. J.; Murray, R. W. *J. Am. Chem. Soc*. **1996**, *118*, 4212. (b) Ingram, R. S.; Hostetler, M. J.; Murray, R. W. *J. Am. Chem. Soc*. **1997**, *119*, 9175. (c) Hostetler, M. J.; Templeton, A. C.; Murray, R. W. *Langmuir* **1999**, *15*, 3782. (d) Templeton, A. C.; Hostetler, M. J.; Kraft, C. T.; Murray, R. W. *J. Am. Chem. Soc*. **1998**, *120*, 1906−1911. (e) Templeton, A. C.; Hostetler, M. J.; Warmoth, E. K.; Chen, S.; Hartshorn, C. M.; Krishnamurthy, V. M.; Forbes, M. D. E.; Murray, R. W. *J. Am. Chem. Soc*. **1998**, *120*, 4845.

(13) (a) Maye, M. M.; Chun, S. C.; Han, L.; Rabinovich, D.; Zhong, C. J. *J. Am. Chem. Soc.* **2002**, *124*, 4958. (b) Maye, M. M.; Luo, J.; Lim, I. S.; Han, L.; Kariuki, N. N.; Rabinovich, D.; Liu, T.; Zhong, C. J. *J. Am. Chem. Soc.* **2003**, *125*, 9906.

(14) (a) Maye, M. M.; Lou, Y. B.; Zhong, C. J. *Langmuir* **2000**, *16*, 7520. (b) Lou, Y. B.; Maye, M. M.; Han, L.; Luo, J.; Zhong, C. J. *Chem. Commun.* **2001**, 473. (c) Luo, J.; Lou, Y. B.; Maye, M. M.; Zhong, C. J.; Hepel, M. *Electrochem. Commun.* **2001**, *3*, 172.

(15) (a) Maye, M. M.; Luo, J.; Lin, Y.; Engelhard, M. H.; Hepel, M.; Zhong, C. J. *Langmuir* **2003**, *19*, 125. (b) Luo, J.; Maye, M. M.; Lou, Y.; Han, L.; Hepel, M.; Zhong, C. J. *Catal. Today* **2002**, *77*, 127.

(16) Luo, J.; Jones, V. W.; Maye, M. M.; Han, L.; Kariuki, N. N.; Zhong, C. J. *J. Am. Chem. Soc.* **2002**, *124*, 13988.

(17) Maye, M. M.; Luo, J.; Han, L.; Kariuki, N.; Zhong, C. J. *Gold Bull.* **2003**, *36*, 75.

(18) Wuelfing, W. P.; Zamborini, F. P.; Templeton, A. C.; Wen, X. G.; Yoon, H.; Murray, R. W. *Chem. Mater.* **2001**, *13*, 87.

(19) Paulus, U. A.; Endruschat, U.; Feldmeyer, G. J.; Schmidt, T. J.; Bonnemann, H.; Behm, R. J. *J. Catal.* **2000**, *195*, 383.

(20) Nashner, M. S.; Frenkel, A. I.; Somerville, D.; Hills, C. W.; Shapley, J. R.; Nuzzo, R. G. *J. Am. Chem. Soc.* **1998**, *120*, 8093.

(21) (a) Galow, T. H.; Drechsler, U.; Hanson, J. A.; Rotello, V. M. *Chem. Commun*. **2002**, 1076. (b) Sun, L.; Crooks, R. M. *Langmuir* **2002**, *18*, 8231.

(22) Yoo, J. W.; Hathcock, D.; El-Sayed, M. A. *J. Phys. Chem. A* **2002**, *106*, 2049.

(23) Acres, G. J. K.; Frost, J. C.; Hards, G. A.; Potter, R. J.; Ralph, T. R.; Thompsett, D.; Burstein, G. T.; Hutchings, G. J. *Catal. Today* **1997**, *38*, 393.

(24) (a) Rolison, D. R. *Science* **2003**, *299*, 1698. (b) Cameron, D. S. *Gold Bull.* **2003**, *36*, 17.

(25) (a) Leibowitz, F. L.; Zheng, W. X.; Maye, M. M.; Zhong, C. J. *Anal. Chem.* **1999**, *71*, 5076. (b) Zheng, W. X.; Maye, M. M.; Leibowitz, F. L.; Zhong, C. J. *Anal. Chem.* **2000**, *72*, 2190.

(26) Han, L.; Maye, M. M.; Leibowitz, F. L.; Ly, N. K.; Zhong, C. J. *J. Mater. Chem.* **2001**, *11*, 1259.

(27) Kariuki, N.; Han, L.; Ly, N. K.; Peterson, M. J.; Maye, M. M.; Liu, G.; Zhong, C. J. *Langmuir* **2002**, *18*, 8255

(28) Han, L.; Luo, J.; Kariuki, N.; Maye, M. M.; Jones, V. W.; Zhong, C. J. *Chem. Mater.* **2003**, *15*, 29.

(29) Derose, J. A.; Revel, J.-P. *J. Microsc. (Oxford)* **1999**, *195*, 64.

(30) Nakaso, K.; Shimada, M.; Okuyama, K.; Deppert, K. *J. Aerosol Sci.* **2002**, *33*, 1061.

(31) Mitchell, C. E. J.; Howard, A.; Carney, M.; Egdell, R. G. *Surf. Sci.* **2001**, *490*, 196.

(32) Weber, A. P.; Friedlander, S. K. *J. Aerosol Sci.* **1997**, *28*, 179.

(33) Campbell, C. T.; Parker, S. C.; Starr, D. E. *Science* **2002**, *298*, 811.

(34) Takano, H.; Kenseth, J. R.; Wong, S.-S.; O'Brien, J. C.; Porter, M. D. *Chem. Rev.* **1999**, *99*, 2845.